PAPER • **OPEN ACCESS**

Study of ion-to-electron temperature ratio at the edge of Wendelstein 7-X using a fast swept ball-pen probe

OPEN ACCESS
IOP Publishing
Plasma Physics and Controlled Fusion
Plasma Phys. Control. Fusion **67** (2025) 115029 (14pp)
https://doi.org/10.1088/1361-6587/ae1b6b

Study of ion-to-electron temperature ratio at the edge of Wendelstein 7-X using a fast swept ball-pen probe

Dario Cipciar[1,*], Jiri Adamek[2], Carsten Killer[1], David Matthew Kriete[3], Victoria Winters[1], Valeria Perseo[1], Olaf Grulke[4], Jiankun Hua[5], Alexander Knieps[5] and the W7-X Team[6]

[1] Max-Planck-Institut für Plasmaphysik, Wendelsteinstr. 1, 17491 Greifswald, Deutschland
[2] Institute of Plasma Physics of the CAS, U Slovanky 2525/1a, 18200 Prague 8, Czech Republic
[3] Auburn University, Auburn, AL, United States of America
[4] Department of Physics, Technical University of Denmark, Lyngby, Denmark
[5] Institute of Fusion Energy and Nuclear Waste Management, Jülich 52425, Germany

E-mail: dario.cipciar@ipp.mpg.de

Received 26 June 2025, revised 7 October 2025
Accepted for publication 4 November 2025
Published 21 November 2025

Abstract

In the Wendelstein 7-X (W7-X) stellarator, a ball-pen probe (BPP) has been routinely employed to measure T_i in the island scrape-off layer (SOL) across large parts of the recent 2024/2025 campaigns. The high temporal resolution of 25 μs allows us to resolve T_i fluctuations, their probability density functions, and modulation via low-frequency magnetohydrodynamics (MHD) modes. We present a unique comparison of the ion temperature measured using BPP with a more conventional retarding field analyzer (RFA). A good agreement between the two diagnostics is observed, when fast T_i measurements are reduced to the same temporal resolution (5 ms) using 'RFA-like' averaging. Using an RFA-like interpretation of the fast BPP data, we find a linear decrease in SOL T_i and T_e with line-integrated density. The SOL ion-to-electron temperature ratio $\tau_{i,e}$ ranges between $\tau_{i,e} = 1$ and 3 with smaller $\tau_{i,e}$ values observed for higher densities (collisionalities) and at positions close to the LCFS. The upstream BPP T_i measurements are compared to the average C^{2+} T_i obtained by coherence imaging spectroscopy (CIS), in the divertor region, magnetically mapped to the BPP. The downstream T_i measured by CIS is about half the upstream T_i and exhibits a similar inverse scaling with line-integrated density. Finally, we benchmark the experimentally obtained SOL T_i and T_e against the EMC3–Eirene modeling and find good agreement for high density plasmas, but significantly diverging results for low density plasmas.

[6] see Grulke *et al* 2024 (https://doi.org/10.1088/1741-4326/ad2f4d) for the W7-X Team.
[*] Author to whom any correspondence should be addressed.

Keywords: ball pen probe, retarding field analyzer, ion temperature, EMC3-Eirene, scrape off layer, island divertor, W7-X

1. Introduction

The scrape-off layer (SOL) is an interface aimed at creating a safe boundary between the core plasma and the machine walls. The Wendelstein 7-X stellarator (W7-X) is utilizing a helically shaped, noncontinuous divertor concept called an island divertor [1, 2]. The low shear design of W7-X generates a small field line pitch $\Theta \approx 0.001$ (poloidal displacement per arc length of the field line to the divertor target inside the divertor islands), which in turn results in long (order of 100 m) field line connection lengths in the island SOL, much longer than in axisymmetric tokamaks not applying resonant magnetic perturbations (RMPs). The island SOL has an intricate 3D shape, comprising regions with different connection lengths (L_c) and incidence angles of the field lines to the divertor targets. Particles and energy entering the SOL from the heated core plasma are transported to the targets using the fastest available transport channels [3]. The targets, referred to as downstream positions, act as sinks for the charged particles, which are either absorbed or recombined to the neutral state and recycled. This creates a pressure gradient that drives parallel flows. However, according to the stellarator two-point model, the long L_c in the island divertor causes the efficiency of perpendicular (cross-field) transport to become comparable to or even higher than that of parallel transport [4]. Therefore, the geometry and position of the magnetic islands affects the performance of the island divertor and the overall performance of the machine [5–8]. In this study, we focus on the 'standard' magnetic configuration, as it represents a center point of the configuration space of W7-X and thus provides a reference case for benchmarking against other configurations or simulations.

With the operation of future power plants in mind, it is essential to keep the erosion of the first wall as low as possible and limit the influx of impurities into the plasma. Monitoring the SOL plasma parameters in front of the plasma-facing components (PFC) is important for understanding the core-SOL interactions and the resulting exhaust of heat and particles into the SOL. Knowledge of the ion temperature (T_i) is needed for ion sound speed and energy flux calculations; the knowledge of which is crucial for the assessment of material erosion of the divertor targets [9, 10]. In this work, using electric probes mounted on a reciprocating manipulator, we characterize the island SOL ion temperature, electron temperature, and density. Ball-pen probes (BPP) [11], capable of measuring ion temperature with high temporal resolution [12], are for the first time employed in the W7-X SOL to improve on the widespread assumption of $T_i = T_e$. The high temporal resolution achieved is necessary for the assessment of ion temperature distribution functions and the sputtering yield, which is highly sensitive to this parameter. As sputtering is a cumulative process, even intermittently increased ion temperatures, when in phase with peak densities, can substantially contribute to the PFC erosion [13]. Time-averaged SOL profiles are useful for obtaining an overview of variations in SOL parameters with varying core plasma parameters. We compare the time-averaged BPP results with a more commonly used retarding field analyzer (RFA) [14, 15], as well as, coherence imaging spectroscopy (CIS) newly optimized for T_i measurement [16, 17]. Unlike in tokamaks, the helical SOL of W7–X makes use of simple 1D models, such as the two-point model [4] imprecise and comparison between two diagnostic systems difficult. To aid in the interpretation of the local data on the complex geometry of the 3D W7-X SOL, we compare the experimental measurements with EMC3-Eirene, which is the leading code on stellarator 3D edge transport modeling [18–21].

2. Experimental setup

To experimentally investigate the ion temperature in the island SOL, probe measurements were conducted with the BPP and an RFA mounted on a reciprocating manipulator and a CIS system close to the divertor surface. The details of these diagnostic systems will be discussed in this section.

2.1. Multipurpose manipulator (MPM)

The MPM is a retractable arm installed in a midplane diagnostic port 15° toroidally from the 'bean-shaped' cross-section of the W7-X. The MPM was built to be a versatile tool for examining the island SOL using a variety of different probe heads [22]. Figures 1(a) and (b) display the typical magnetic structure of the SOL in terms of the distribution of target-to-target connection length ($L_c = L_{c,+} + L_{c,-}$) at the MPM location. The insertion path of the MPM is depicted as white lines. Two different configurations are shown: a 'Standard' configuration in figure 1(a) and a 'High mirror' configuration in figure 1(b). Both configurations have $\iota = 1$ at the LCFS and therefore five islands in the SOL. In this paper, for the standard configuration, we distinguish three topological regions of the SOL along the MPM path (highlighted in figure 1(a)): 1. The near LCFS region is localized ($R - R_{LCFS} \leqslant 2$ cm) from the LCFS and characterized by $L_c > 250$ m; 2. The main island SOL is localized near the island center and characterized by intermediate $L_c = 250$–350 m; 3. The target shadow region (TSR) is the furthermost edge region characterized by the shortest connection lengths (< 50 m), where the field lines intercept the targets before completing one revolution around the torus.

A high mirror configuration was selected (in addition to the standard configuration), based on T_i data availability from SOL probes. For the studies discussed in this paper, two different probe heads, the 'IPP–FLUC3' and

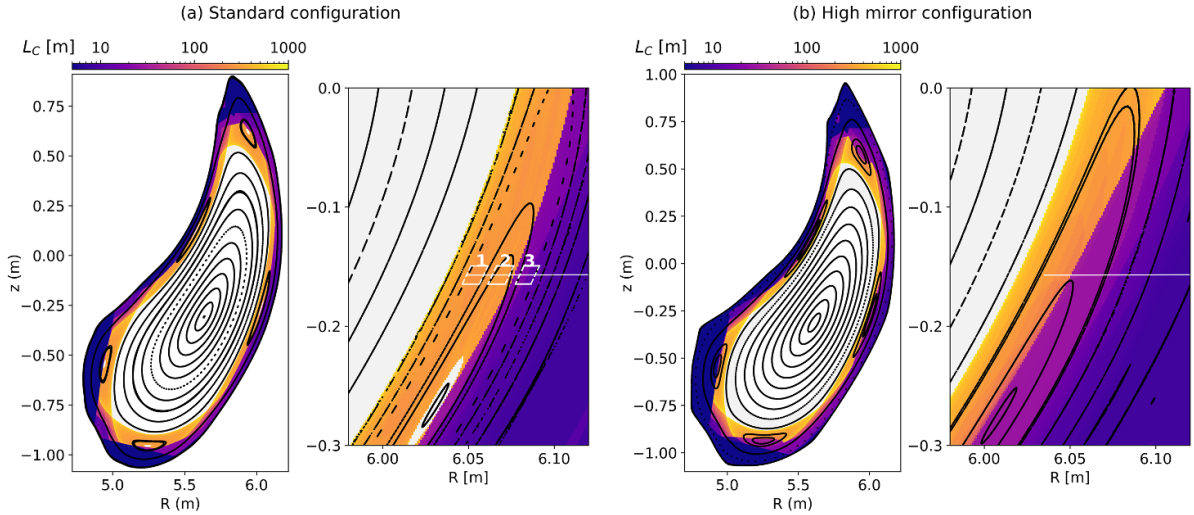

Figure 1. Full cross-section and zoomed-in Poincaré plot with 2D connection length of magnetic field lines color-coded at the location of MPM ($\phi = 200.8°$) in (a) standard configuration and (b) high mirror magnetic configuration. A typical insertion path is shown as a white line; white polygons correspond to SOL regions along the BPP path, which are referred to in further analysis.

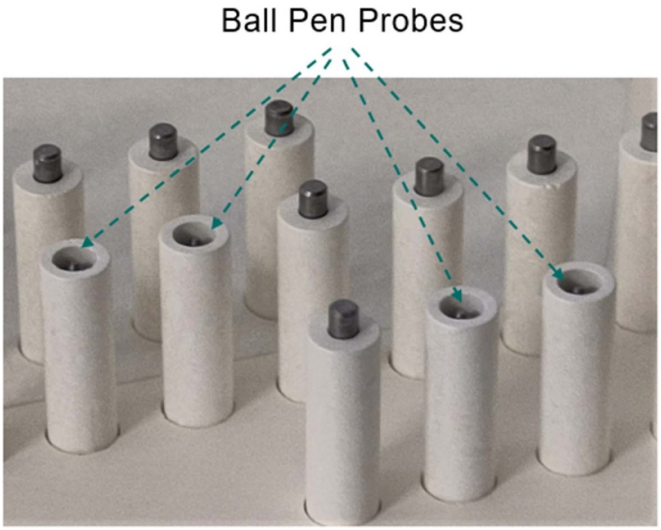

Figure 2. IPP–FLUC3 probe head with Langmuir probes (diameter $d = 2\,\text{mm}$, length $l = 2\,\text{mm}$) and Ball pen probes ($d = 3\,\text{mm}$, retraction $h = -0.5\,\text{mm}$).

'FZJ–RFA2' were used in complementary discharges in these two configurations.

The probe head 'IPP–FLUC3' was built to study turbulence in W7-X SOL [23]. The body of the probe head is made out of high purity boron nitride ceramic. Langmuir probes mounted on the front panel of the probe head are constructed from 3-cm-long tungsten wires with $d = 2\,\text{mm}$. The wires are placed into slim BN shielding tubes, such that, only the last 2 mm of length (collector) of each of the tungsten wire contacts the plasma, as shown in figure 2. This design is intended to reduce the impurity release (boron, nitrogen) from the body of the probe into the plasma by keeping the primary body of the probe further away from the point of measurement. Triplets of such Langmuir probes form a triple probe (TP) and are used to directly calculate the electron temperature (T_e) and electron density (n_e) using the TP model, assuming a Maxwellian distribution of electron energy. Langmuir probes are intrinsically incapable of measuring the ion temperature (T_i), which is notoriously challenging to obtain. For T_i to be measured with electric probes, ions must be collected by applying varying (swept) positive (retarding) fields. This comes at the expense of inflicting large electron currents on to the probe. These currents, naturally, must be eliminated by the probe design. Up to this date, only a few diagnostics have been systematically used for T_i measurements in SOL, namely, the RFA [14, 15, 24], the BPP [12, 25], and impurity Doppler spectroscopy using coherence imaging method [17, 26, 27]. The BPPs on W7-X have been designed to fit the construction of the probe head 'IPP–FLUC3' without significantly reducing its other capabilities [23]. Typically, BPPs are embedded in the graphite body of a probe head; however, in our case, the BPPs are proud, extending from the main probe body, similarly to the Langmuir probes (figure 2). Proud BPPs are constructed out of a boron-nitride shielding tube with an inner diameter of $d = 3\,\text{mm}$ and a conical tungsten collector with a diameter of 2 mm, which was retracted into the shielding tube by $h \approx -0.5$ mm. The retraction depth was calculated to be approximately equal to the ion gyration radius, given the expected SOL background temperatures $T_e \approx T_i \approx 30$ eV to screen-off the parallel electron flux while retaining the ion flux. This allows us to apply a high positive voltage to the shielded collector. The measurement of ion temperature is obtained by applying swept (variable) voltage and measuring the collector current (I_{coll}). The sweeping frequency is limited by the measurement electronics, most importantly by the data acquisition system sampling at 2 MHz, but also by the length of the signal transmission line before the amplifier. With everything considered, the sweeping frequency of BPP was selected as $f = 20\,\text{kHz}$ (sweep period: $50\,\mu\text{s}$), with a bandwidth of useful signal (harmonic frequencies) up to 140 kHz.

Figure 3. FZJ–RFA2 probe head with Langmuir probes (diameter $d = 2\,\text{mm}$, length $l = 2\,\text{mm}$) on front face and RFA entrance slits on a side.

The probe head 'FZJ-RFA2' [15], shown in figure 3, was built to measure the ion temperature in W7-X SOL. The boron-nitride body of the probe comprises two identical rectangular openings on opposing sides (side A and side B), which are aligned with the direction of the toroidal magnetic field. Behind the entrances are biased slits and grids intended to: 1. Screen-off thermal electrons with negative bias, 2. Selectively retard the ions by varying (sweeping) the positive voltage of the grid (V_{grid}), and 3. Screen-off any remaining electrons with negative bias, respectively. A fraction of the incidence ion flux is transmitted to the collector plate behind the grids and measured as the collector current (I_{coll}). The distribution of ion energies is, similarly to the BPP, obtained from the dependence of the collected current on the swept positive voltage applied to the ion retarding grid. In addition, a triple Langmuir probe is installed on the front plate of the RFA probe head for measuring the electron temperature and density. Notably, as the TP of the RFA probe head is located at the top of the probe, which is 1 cm deeper than the RFA analyzer slits, the maximum depth of insertion of the probe head is limited by the melting point of the Langmuir pins (figure 3). The maximum sweeping frequency of the grids is limited by the capacitive currents in the signal transmission lines and to bias sources and between the RFA grids. The maximum sweeping frequency used in the MPM was therefore selected as $f = 1\,\text{kHz}$. The collector current is typically on the order of mA and, for this sweeping frequency, the capacitive current is ($\approx 10\,\mu\text{A}$). Due to the strong fluctuations of the collector current, multiple *IV* curves are typically averaged together, achieving an effective temporal resolution of 3–5 ms.

2.2. Coherence imaging spectroscopy

Coherence imaging spectroscopy (CIS) [16] is a diagnostic recently upgraded for measuring high spatial resolution 2D images of the C^{2+} impurity ion temperature in the divertor plasma of W7-X. Thanks to crystals specially designed to resolve the fine structure of spectral lines despite Doppler broadening, the T_i information can be obtained. Since W7-X divertor targets and other PFCs are made of graphite, the C III 465 nm spectral line is used for T_i measurement, as it is among the brightest ones. The T_i derived from this line is representative of the T_i of the main ion species, due to the relatively short thermal equilibration time (0.01 ms–1 ms) between C^{2+} and H^+ ions [16] as compared to the transport timescale $\approx 10\,\text{ms}$ [28] and the lifetime of the C^{2+} charge state [29]. Figure 4 shows the magnetic topology near the lower divertor target in the CIS field of view (FoV) for the standard magnetic configuration. The MPM path mapped onto the CIS FoV is depicted as circles.

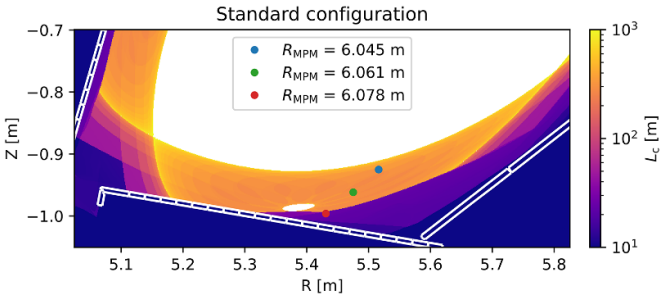

Figure 4. Connection length distribution at cross-section in the CIS field of view. Colored markers indicate field lines mapping to the MPM position. Divertor PFCs are shown in white.

2.3. The BPP fast sweeping method

The BPP current–voltage (*IV*) curves were obtained by sweeping the collector between $-110\,\text{V}$ and $+190\,\text{V}$. Therefore, for a typical scenario, where the plasma potential ϕ is in the range 0–100 V, the BPP measures both the ion and electron saturation currents $I_{\text{sat,i}}$ and $I_{\text{sat,e}}$, respectively. The measurement of the whole I–V curve is beneficial for a multitude of reasons. First, it is necessary to find the electron-to-ion saturation current ratio $\mathcal{R} = \frac{I_{\text{sat,e}}}{I_{\text{sat,i}}}$, characteristic for the BPP used. Second, it enables us to reliably determine the BPP floating $V_{\text{fl,BPP}}$ and plasma potential Φ in a wide range of plasma conditions ($V_{\text{fl,BPP}}$ can be negative). Third, the electron temperature can be obtained from the ion branch fit as a byproduct. Disadvantages of full *IV* measurement are presented as follows: the success of the electron branch fit (T_i measurement) relies on the success of ion branch fit; reduced maximum achievable temporal resolution, due to DAQ sampling limitation; and lower maximum achievable positive voltage, due to amplifier voltage limitation. As the frequency of the collector voltage sweeping was set to 20 kHz, capacitive currents arise due to signal lines before the amplifier. To remove the parasitic current from I_{coll} signal, we model the capacitive current as $I_{\text{cap}} = C\frac{\text{d}V_{\text{coll}}}{\text{d}t} + \text{const}$. After digitally subtracting the stray (I_{cap}) current and limiting the frequency bandwidth with a third-order Butterworth lowpass filter with a cutoff at $f < 140\,\text{kHz}$, the remaining stray current is $\approx \pm 0.01\,\text{mA}$, delivering good signal-to-noise ratio (SNR) relative to the typical I_{coll} in the order of mA. Having an SNR of two orders of magnitude makes the error, which stems from the stray current,

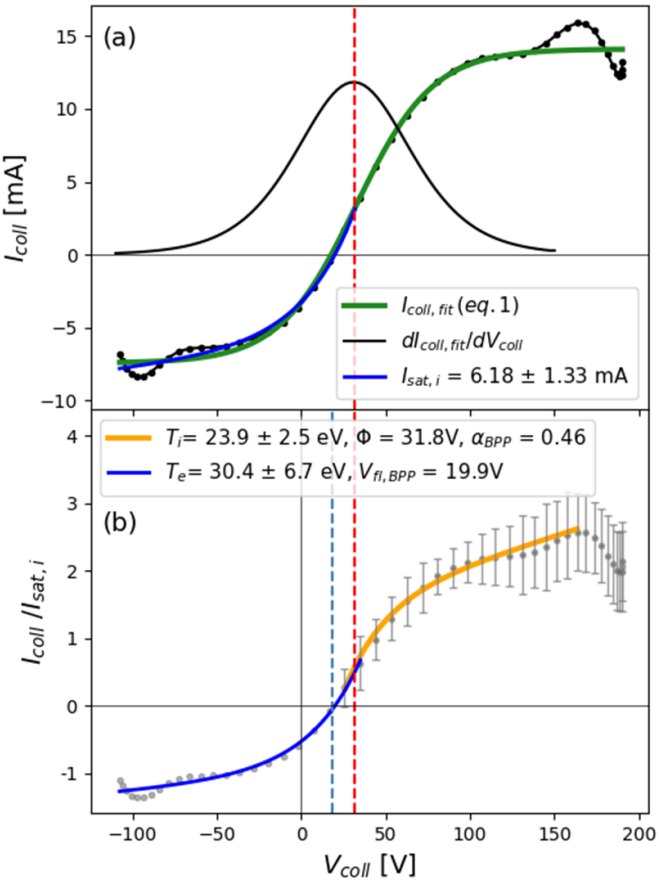

Figure 5. Single *IV* characteristic of BPP, with (a) I_{coll} in mA and (b) I_{coll} normalized to I_{sat}^{+}. The estimated plasma parameters are $\Phi = 31.8\,\mathrm{V}$ (black dashed lines), $T_{\mathrm{i}} = 23.9 \pm 2.5\,\mathrm{eV}$ and $T_{\mathrm{e}} = 30.4 \pm 6.7\,\mathrm{eV}$.

negligible. Figure 5(a) displays a typical (sweep half-period of 25 μs) *IV* characteristic of BPP on W7-X, following the noise removal. The plasma parameters are obtained by curve fitting performed in a couple of steps, starting with an estimation of the plasma potential Φ. To obtain the plasma potential, the entire *IV* curve (black dots in figure 5(a)) is first fitted by a single function:

$$I_{\mathrm{coll}}(V) = A\frac{1-e^{\chi}}{1+Ce^{\chi}(1-\mathcal{D}\chi)}, \chi = \frac{V-V_{fl}}{B}, \qquad (1)$$

where the floating potential (V_{fl}) represents the voltage, where $I_{\mathrm{coll}}(V_{\mathrm{coll}}) = 0$. The remaining minimized coefficients A, B, C, D do not have a meaningful physical interpretation for the BPP *IV* characteristics. The result of the dataset interpolation with equation (1) is the green curve shown in figure 5(a). The first derivative of the smooth green curve $\mathrm{d}I_{\mathrm{coll,\,fit}}/\mathrm{d}V_{\mathrm{coll}}$ is depicted as a black curve, which is plotted for illustration in arbitrary units. The inflection point, for example, the voltage where the second derivative of the smooth green curve $(\mathrm{d}^2I_{\mathrm{coll}}/\mathrm{d}^2V_{\mathrm{coll}} = 0)$, defines the plasma potential Φ (red dashed line), which will be fixed in the following steps. Second, the ion saturation current ($I_{\mathrm{sat,i}}$) obtained from a four-parameter fit [25, 30] below the plasma potential $(V < \Phi)$ is shown as the blue curve in figure 5(a). The ion saturation current is used to normalize the *IV* characteristic to $I_{\mathrm{sat,i}} = 1$. The normalized *IV* characteristic is shown in figure 5(b) as gray points. For illustration, the ion branch fit of normalized *IV* is also shown in figure 5(b). The electron branch of the normalized *IV* curve is fitted with equation (2) [12]:

$$I_{\mathrm{coll}}(V_{\mathrm{coll}}) = \mathcal{R}(1+k(V_{\mathrm{coll}}-\Phi)) - \mathrm{e}^{\frac{\Phi-V_{\mathrm{coll}}}{T_{\mathrm{i}}}}, \qquad (2)$$

where the estimated parameters are the ion temperature T_{i}, the ratio of electron to ion saturation current $\mathcal{R} = I_{\mathrm{sat,e}}/I_{\mathrm{sat,i}}$, where $I_{\mathrm{sat,i}} = 1$. The electron saturation current was previously observed to increase linearly with the probe bias [12] and has also been reproduced in PIC simulations [31]. Considering nonsaturation, a parameter k is introduced, which defines its slope. With equation (2) fit, we can estimate $\mathcal{R}$ as the current saturation value at the plasma potential ($V_{\mathrm{coll}} = \Phi$), without the need to linearly interpolate the currents to the plasma potential. Moreover, each datapoint of the electron branch is given a weight factor $w = 1/\sigma$, calculated from a standard deviation (σ) of the measured current during a 1 ms interval, shown as an errorbar. Typically, σ increases with positive voltage; thus, the relative weight of datapoints decreases. To ensure that turbulent density perturbations near the maximum positive voltage do not affect the fit, a cut-off fitting is used, where the upper voltage range (V_{cutoff}) for fit is varied within ($\Phi < V_{\mathrm{cutoff}} \leqslant V_{\mathrm{coll,max}}$ and the most stable fit is selected). The resulting fit of the electron branch with equation (2) is shown as the orange curve in figure 5(b). The voltage range for the fit was selected by the algorithm as ($\Phi = 32\,\mathrm{V}$ to $V_{\mathrm{cutoff}} = 160\,\mathrm{V}$).

The results of the *IV* fits are shown in figure 5, from which the working principle of the BPP can be verified. First, the *IV* curve is nearly symmetric (electron and ion currents at the collector are well balanced) with $\alpha_{\mathrm{BPP}} = \ln\mathcal{R} = 0.46$, which is in the typical range found in other devices [11]. Second, the BPP floating potential $V_{\mathrm{fl,BPP}} = 20\,\mathrm{V}$ is close to the plasma potential $\Phi = 32\,\mathrm{V}$, and with the estimated electron temperature $T_{\mathrm{e}} = 30\,\mathrm{eV}$, thus fulfilling the equation:

$$\Phi = V_{\mathrm{fl}} + \ln(\mathcal{R})T_{\mathrm{e}}, \qquad (3)$$

as expected from the probe theory [32].

3. Temporal evolution of SOL parameters

Although sweeping electric probes at high frequencies is a challenging task, the fast measurements were revealed to be desirable for an adequate description of the turbulent SOL plasma by both the RFA and BPP techniques [33, 34]. Nevertheless, ion temperatures are to this day rarely measured with sufficient temporal resolution. Following the approach presented in the previous section, we perform a fit to obtain T_{i} value every 25 μs. However, instances of even faster ($<$25 μs) turbulent density perturbations can occur and significantly increase the uncertainty of the fit. Therefore, only fits with all fitted parameters not exceeding the relative error of 60% are used in the further analysis.

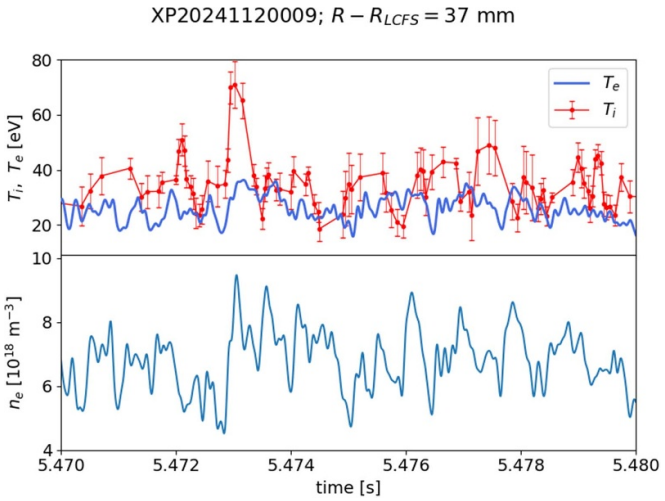

Figure 6. Example time trace of fluctuating SOL parameters T_i, T_e, n_e measured in the TSR region.

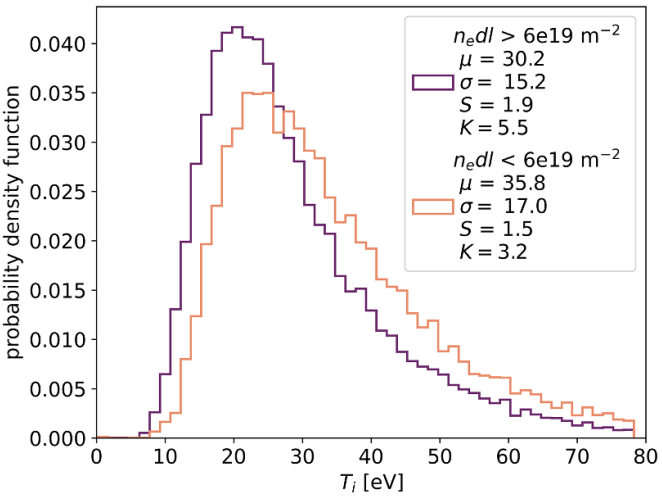

Figure 7. Ion temperature histograms in SOL region $R - R_\mathrm{LCFS} =$ 3.5–4.5 cm, compiled from 89 standard configuration discharges. The effect of line-integrated central density on T_i is distinguished for a case below (orange) and above (violet) $n_\mathrm{e}\mathrm{d}l = 6 \times 10^{19}\,\mathrm{m}^{-2}$.

Figure 6 presents an example of fluctuations of local SOL parameters T_i, T_e, and n_e obtained from a discharge in a high mirror configuration with an input electron cyclotron heating power $P_\mathrm{ECRH} = 2.5$MW and line-integrated central density $n_\mathrm{e}\mathrm{d}l = 4 \times 10^{19}\,\mathrm{m}^{-2}$. The T_e and n_e signals are lowpass filtered to $f = 10$ kHz and T_i is sampled at an effective frequency of 10 kHz. The probe head at the instance of measurement was positioned ≈37 mm from the LCFS in the TSR with short connection lengths $L_\mathrm{c} < 50$ m. We observe that the fluctuations of ion temperature are of different nature from those of electron temperature. Although T_e oscillates around its mean value, T_i exhibits intermittent character. Using fast Fourier transform (FFT) cross-spectral analysis, we have observed that the local SOL density n_e fluctuations during this 10 ms time interval can reach up to ≈65% cross-coherence with T_i fluctuations with a phase shift of $\pi/2$. Moreover, we observe that T_i fluctuates between the cold background value, equilibrated with the local T_e, and intermittent high T_i values, which exceed the ones of T_e by up to a factor of 4. The ion dynamics (strongly elevated T_i values) may be attributed to the difference in parallel conductivity of ions and electrons, scaling as $\sqrt{m_\mathrm{i}/m_\mathrm{e}}$, resulting in the parallel ion energy loss to be much lower than the electron one. A similar behavior was previously observed with fast T_i measurements in tokamaks [33, 34] and simulations of ion dynamics [35].

The observations made from figure 6 can be generalized using a statistical approach to analyze intermittent signals in the same SOL region. Probability density functions (PDFs), shown in figure 7, were applied for better statistics calculated from a database of 89 standard configuration discharges. As this database comprises discharges with various plasma parameters, it provides a very robust approach, intended to provide an overview of T_i probabilities at the location closest to the PFCs, where the BPP still has sufficient signal. The ion temperatures in the SOL of tokamaks are observed to have a dependency on line-integrated density [24, 34, 36]. Therefore, the database of discharges used for this analysis was separated into two groups, based on the central line-integrated density being lower or higher than $n_\mathrm{e}\mathrm{d}l = 6 \times 10^{19}\,\mathrm{m}^{-2}$. We observe that $n_\mathrm{e}\mathrm{d}l$ does affect the parameters of the PDF, where the low-density PDF is shifted toward higher ion energies at the same SOL position. This will be investigated in more detail in the following sections. Apart from the shift, the PDFs show a non-Gaussian shape, peaking at low $T_\mathrm{i} \approx 30$ eV, attributed to the background plasma, and a hot tail with T_i up to ≈80 eV, attributed to nonequilibrium ion temperature fluctuations. Similar observations of non-Gaussian T_i PDFs were made on tokamaks [12, 33, 37], where the statistical moments were shown to be in good agreement with the gamma and beta distribution function in [34].

Although the W7-X SOL is intrinsically free of radially propagating filamentary structures or blobs [38], of particular interest are the low-frequency $m = 1$ magnetohydrodynamics (MHD) modes, which were observed to originate in the plasma outer core $0.5 < r/a < 1$ [39]. The presently achieved T_i temporal resolution of 25μs allows for the measurement of fluctuations in the SOL during the quasicontinuous (QC) low-frequency modes, which typically occur in low power, low density plasmas with a frequency $f = 500$ Hz. Figure 8 shows a time trace of SOL parameters T_i, T_e, and n_e during 500 Hz mode activity in a standard configuration measured in a private flux region of the SOL, 39mm away from the LCFS. We observe that the fast T_i values are modulated by the QC mode, such that, they become approximately in phase with T_e. Due to the MHD character and the large spatial structure ($m = 1$) of the mode, the SOL measurements are correlated with segmented Rogowski coils [40], sensitive to changes in poloidal magnetic flux. Although T_i can still exceed the peak T_e values with $\tau_\mathrm{i,e} = 1$–3, neither the peak nor the background values of T_i were observed to be significantly increased when compared to discharges without the QC mode activity. This is in line with expectations, as the QC oscillations in the standard configuration are not known to be strongly detrimental to the

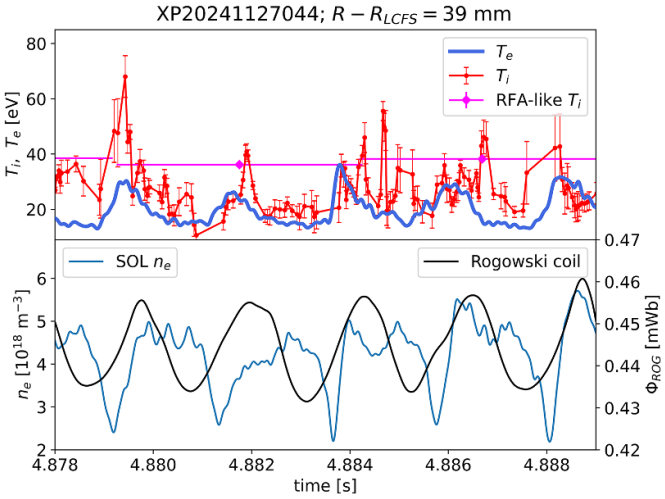

Figure 8. Fluctuations of SOL parameters (T_i, T_e, n_e) modulated by $m = 1$ MHD $f = 500$ Hz mode activity in the outer core of W7-X.

confinement [39]. We conclude that the QC modes modulate the T_i fluctuations in terms of phase, such that T_i and T_e can become in phase with Rogowski signals, related to the minima and maxima of the QC mode. In the following sections, we will introduce 'RFA-like' temporal averaging technique, useful for the interpretation of the fast T_i data. The 'RFA-like T_i' 5 ms time averages are already included in figure 8.

3.1. The RFA and 'RFA-like' methods

The RFA probe typically measures the ion temperature profiles with low (1 up to 5 ms) temporal resolution [15, 24]. It was shown in [33] that the resulting RFA ion temperature does not depend on the RFA sweeping frequency. However, it does depend on the choice of fit boundaries. This dependency is shown to be due to the effect of ion temperature fluctuations, having a non-Gaussian PDF [33] (as was also explained in section 3). In this work, we choose the 'classic' RFA fit of the whole *IV* characteristic, consistent with previous RFA measurements on W7-X [14, 15]. Such a fit provides us with an I_{sat} and Φ weighted average while still being a conservative estimate of T_i. The RFA fit gives more weight to those T_i values, which have higher I_{sat} and/or Φ. Hence, the resulting RFA T_i average does not neglect the contribution of the hot tail of the T_i distribution function. The RFA measures an ion current (incident flux of ions) reaching the collector, which follows an exponential decay with the positive voltage applied V_{grid}, which can be expressed as follows:

$$I_{coll} = \begin{cases} I^{+}_{sat}, & V_{grid} < V_s \\ I^{+}_{sat} e^{-\frac{Z}{T_i}(V_{grid} - V_s)}, & V_{grid} > V_s, \end{cases} \quad (4)$$

where the sheath potential $V_s \approx 3T_e$ is measured directly from the characteristics as a difference between vessel and plasma potential Φ. In the following, the RFA Φ is defined by the 'knee' potential of its *IV* characteristic. The ion temperature

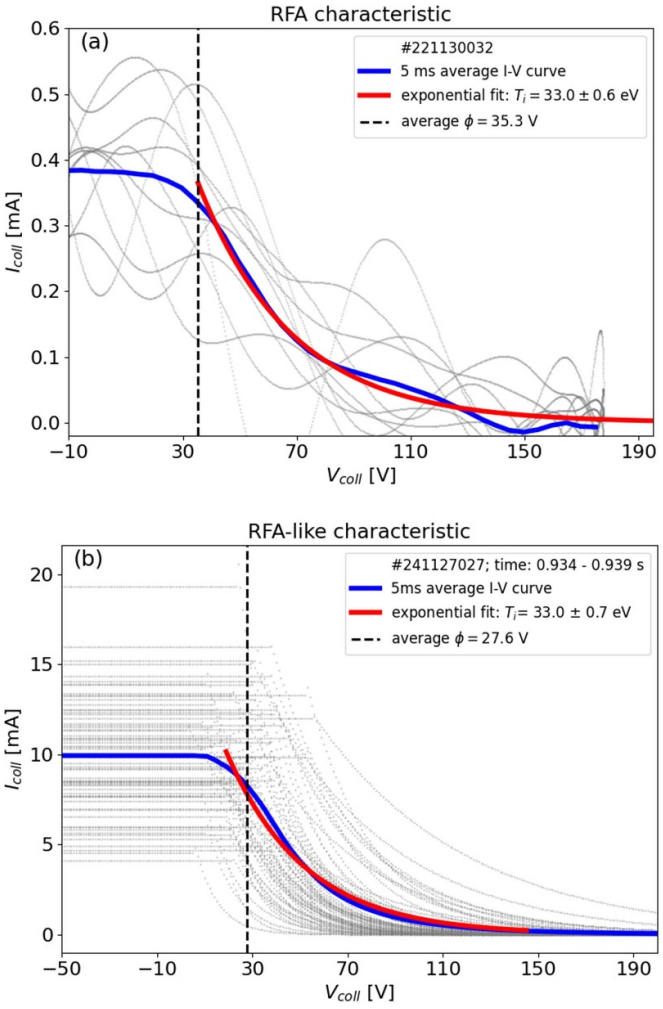

Figure 9. (a) RFA *IV* characteristic measured during a program XP20221201042. Five curves (5 ms) are averaged together (blue line) and fit with equation (4) (red curve). (b) RFA-like *IV* characteristics (dashed gray lines) reconstructed from fast swept BPP results measured during a program XP20241120009. Time-averaged *IV* curve (blue line) is fitted with the RFA model equation (4) (red curve) to obtain the 5 ms average T_i value.

(T_i) is calculated assuming that the incident flux is dominated by hydrogen ions ($Z_i = 1$) and assuming Maxwellian distribution of parallel ion velocity. Typical RFA *IV* characteristics measured on W7-X are shown in figure 9(a) as gray lines. These are due to signal noise, typically averaged over 5 ms time intervals (blue curve) before fitting. We observe that the collector current, devoid of electron current contribution, remains constant in the range $0 < V_{grid} < \Phi$, as described by equation (4). The T_i is inferred from an exponential fit according to equation (4) (red curve). The same process is repeated for both sides (A, B) of the RFA probe. The final T_i value is obtained as $T_i = (T_{i,A} + T_{i,B})/2$, as is typically employed to obtain a single RFA measurement [41, 42].

Figure 6 shows that the fast BPP T_i data have an intermittent character with a non-Gaussian distribution. A simple mean of such T_i data would present an underestimate of the

intermittent high T_i structures, biased toward the cold SOL background, typically $T_i \approx 20$–30 eV even in the deepest probe insertions. The 'RFA-like' method [12], analogously to the RFA probe method, can be used to interpret the BPP obtained fast T_i fluctuations, giving a higher 'weight' to those T_i measurements, which also have a higher effective signal ($I_{sat,i}$) and a higher positive plasma potential (Φ). The method is performed by reconstructing (emulating) the RFA *IV* characteristics prescribed by equation (4) using the fast (25 μs) BPP results: T_i, Φ, $I_{sat,i}$. Such emulated *IV* characteristics are shown as gray lines in figure 9(b). The individual reconstructed *IV* characteristics are, similarly to the RFA, averaged over time to achieve the desired temporal resolution, in our case, the one of the slow swept RFA (5 ms). A fit (red curve) of the average IV characteristic (blue curve) is shown in figure 9(b). Note that since the emulated (synthetic) IV characteristics are without signal noise, the fit covariance is low, giving a small errorbar typically <1 eV.

4. Comparison of BPP and RFA radial profiles

The operation of the BPP and RFA in similar magnetic configurations in W7-X offers a unique opportunity to compare the findings of these two vastly different probe heads. Following the RFA-like approach, described in the previous section, we average the BPP fast T_i measurements to match the temporal resolution of the RFA (5 ms). To make the comparison more robust, two pairs of complementary discharges were chosen. One pair of medium density discharges in a high mirror magnetic configuration is shown in figure 10 and the second pair in high density discharges in the standard magnetic configuration, shown in figure 11. Note that the probe heads operated in similar but not exactly the same magnetic fields and slightly different densities. For this reason, a slight difference in the width of the SOL is visible in the T_e profiles (blue dotted and solid lines). This is likely due to a small difference in the iota profile between the two pairs of discharges. The iota causes a slight inward shift of the T_e profiles and wider magnetic island in the case with RFA-probe head. The slight misalignment of the discharge parameters is currently not avoidable due to a lack of RFA data availability. Note that the triple Langmuir probe on the RFA probe head has a large separation of the Langmuir pins, which is not optimal and can cause issues, such as the unphysical drop of T_e at the deepest probe insertion in figure 11. Despite this, the triple Langmuir probe T_e profiles achieve a relatively good agreement, and the core plasma parameters are similar; thus, we can consider the discharges complementary.

The resulting time-averaged RFA and RFA-like ion temperature profiles show good agreement between the two probes and flat T_i profiles, in both configurations. Moreover, the impact of the density is readily visible on the profiles, where the higher density discharge shows lower values of T_i and T_e. With gray color, we also display a simple mean value of the fast BPP T_i data, representing values, biased toward background (most probable) T_i as previously observed on tokamaks [12, 33, 37].

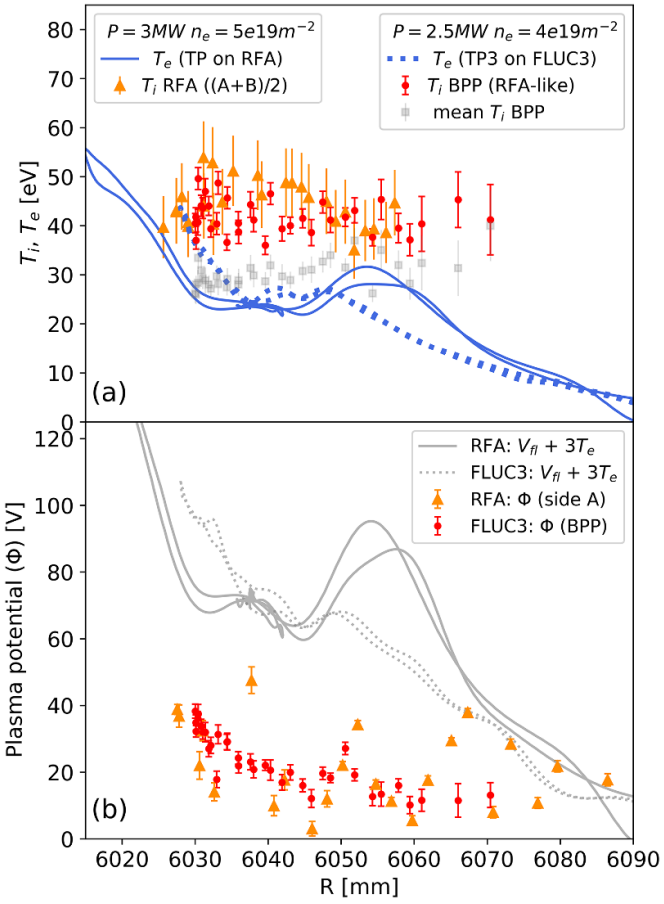

Figure 10. High mirror magnetic configuration. Comparison of FLUC3 and RFA probe radial profiles from two complementary discharges (XP20241120009 and XP20221201042), showing: (a) T_i radial profiles measured with the BPP (RFA-like method and simple mean), the RFA probe head and T_e measured with triple Langmuir probes; (b) plasma potential radial profiles measured with BPP, RFA, and Langmuir probes.

The good agreement between RFA and BPP indicates that the parallel ion energies (average of both RFA sides) and perpendicular ion energies (measured by BPP) are similar. The $\tau_{i,e} = T_i/T_e$ ratio ranges between 1 and 3, where $\tau_{i,e} = 1$ (thermalization) is obtained at the deepest probe insertion ($\approx$1 cm from the LCFS), where the T_e gradient typically steepens up and intersects with the T_i profile. Similar observations were made in tokamak SOLs, where $\tau_{i,e} = 1$ would be reached at the LCFS [12] or even slightly deeper inside the confined region [24]. As a byproduct, a very good agreement was observed between the RFA and BPP measured plasma potential (Φ) in both configurations, shown in figures 10(b) and 11(b). The plasma potential is an important parameter for the RFA fit, as it defines the break-point between saturation and the exponential decay of the incident ion current from which the T_i is obtained. Thus, it serves as a further proof of equivalency of the two probe measurements. In addition, comparing the RFA or BPP potential with a plasma potential profile estimated using a Langmuir probe relation $\Phi = V_{fl} + 3T_e$, shown as gray lines in figures 10(b) and 11(b), we find a significant disagreement. The reason for this mismatch is currently

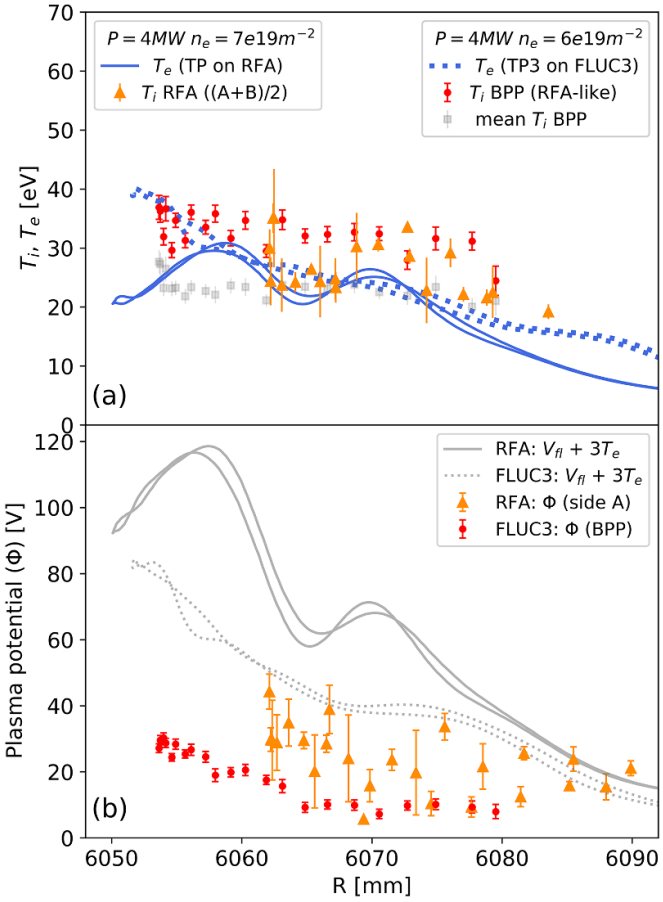

Figure 11. Standard magnetic configuration. Comparison of FLUC3 and RFA probe radial profiles from two complementary discharges (XP20241127027 and XP20221130032), showing: (a) T_i radial profiles measured with the BPP (RFA-like method and simple mean), the RFA probe head and T_e measured with triple Langmuir probes; (b) plasma potential radial profiles measured with BPP, RFA, and Langmuir probes.

not understood and is being further investigated, as it is relevant for the understanding of radial electric fields and drifts in the SOL.

5. Scaling of SOL temperatures with line-integrated central density

In this section we present the results of measurements comprise 344 probe plunges from 89 discharges in the most commonly used configuration, the standard magnetic configuration. For this analysis, the BPP fast T_i data were time averaged using the RFA-like technique on 5 ms time scale in three regions of the island SOL. Based on the MPM database, a subset of nine representative discharges were selected for CIS C^{2+} T_i analysis in the divertor region (downstream). To account for the 3D geometry of W7-X, the field line tracing code was used to map the MPM insertion path into the CIS 2D field of view. The mapping is depicted in figure 4.

Figure 12 shows the average SOL T_i and T_e data, plotted as a function of central line-integrated density $n_e dl$, with the heating power $P_{ECRH} + P_{NBI}$ color-coded. Note that all of the discharges are ECR heated with only a minority NBI heating $P_{NBI} < 1.5$MW. In this study, the SOL is separated into three locations based on the relative distance between LCFS and the local connection length between nearest divertor targets in a standard configuration. The near LCFS location (figures 12(a) and (b)), is here defined as 1 cm–2 cm from LCFS with $L_c > 250$ m and the main island SOL (figures 12(c) and (d)), is typically located 2.5–3.5 cm from LCFS with $350 > L_c > 250$ m. Due to the long connection lengths, these two regions can be considered as the 'upstream' of divertor targets. The field lines of these regions are connected to the divertors observed by the CIS system. The TSR (figures 12(e) and (f)) is in a standard configuration located 4 cm–5 cm from the LCFS. The TSR region is a portion of the island cut by divertor targets with only short connection lengths $L_c < 50$ m. The SOL regions were identified using a field line tracing code that calculated connection lengths, considering the changes in island magnetic topology due to toroidal plasma current and the changes in the LCFS position. For better statistics, individual measurements (probe insertions) are averaged over these 1 cm spatial intervals (regions). The CIS downstream T_i was computed by taking an average over the region in the CIS images where the MPM field lines pass and for toroidal angles of 133°–135°, where the CIS Ti data have the lowest error. This averaging presents a rough estimate for the average downstream ion temperature, given the uncertainty in the radial location of CIS measurements. This uncertainty is due to the line-integrated nature of CIS measurements, where the measurement is localized to a narrow range of electron temperatures for which C III emission occurs [16]. The CIS currently cannot discern the vertical position of this C III emission zone (T_i measurement), which is likely localized to a particular position slightly above the divertor. Therefore, we cannot well discern the downstream regions corresponding to individual upstream regions; hence, averaged CIS data are compared to all three upstream regions, shown in figures 12(a), (c), and (e).

The local SOL T_i plotted in figures 12(a), (c), and (e) is observed to increase linearly with the decrease in line-integrated density in all of the SOL regions. In the range of line-integrated densities $n_e dl = (2\text{–}10) \times 10^{19}\,\mathrm{m}^{-2}$ the SOL T_i decreases by a factor of ≈1.5. A similar linear trend is observed with the CIS system, where downstream T_i decreases within the same density range by a factor of ≈1.5. Quantitatively, the upstream ion temperatures in figures 12(a), (c) are systematically higher by a factor of ≈2 from the downstream ones measured by CIS and by a factor of ≈1.5 higher in the TSR region (figure 12(e)). A quantitative agreement is not to be expected due to a number of reasons, such as much higher impurity cooling near the divertor target, the requirement of thermal equilibration of C^{2+} with the main ion species and parallel temperature gradient. The exact reason for the quantitative difference is yet to be studied. We note that, at least at high density, the downstream ion temperature is surprisingly smaller with higher heating power. This is related to a change in the C III emission distribution with power, which is related to the measurement location (related to T_e) changing in the SOL.

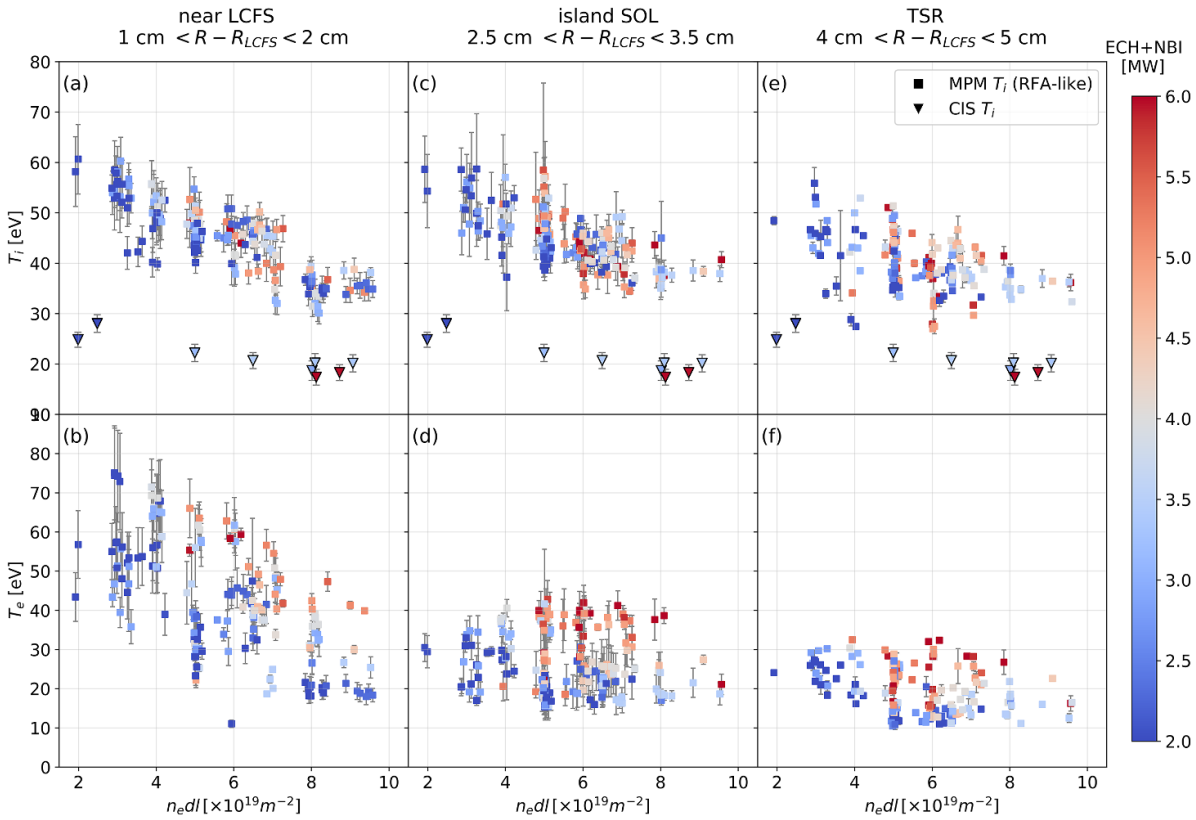

Figure 12. Scaling of averaged local T_i and T_e with the line-integrated density $n_\mathrm{e}\mathrm{d}l$, measured with BPP (RFA-like) and Langmuir probes at three island SOL locations (squares) and C^{2+} T_i measured with CIS system downstream at a divertor target (triangles). The color corresponds to the total input heating power.

The local SOL T_e, plotted in figures 12(b), (d), and (f), decreases with the line-integrated density, particularly in near the LCFS region. In further regions of the SOL (main island SOL and TSR) T_e responds only weakly to the change of $n_\mathrm{e}\mathrm{d}l$. In the main island SOL region, the T_e profiles can be radially nonmonotonic (hollow), especially in low density plasmas ($n_\mathrm{e}\mathrm{d}l < 5 \times 10^{19}\,\mathrm{m}^{-2}$) in the island SOL [43–45]. In the density range ($n_\mathrm{e}\mathrm{d}l = 7$–$10\,\mathrm{m}^{-2}$), a factor of 2 increases of T_e with the input heating power is clearly visible. This increase likely stems from a decrease in the temperature profile hollowness, likely due to increased turbulent cross-field transport, related to the local electron pressure gradient ∇p increase [46]. Interestingly, the SOL T_i is less affected by the ECRH heating power. We observe that the SOL ion-to-electron temperature ratio $\tau_\mathrm{i,e}$ depends on multiple parameters, such as, the line-integrated density, heating power, and also the SOL region. Therefore, we can conclude that $\tau_\mathrm{i,e}$ ranges between 1 and 3 in the island SOL and $\tau_\mathrm{i,e}$ in general converges to unity in the near SOL region.

6. Comparison of measured SOL parameters with simulations

6.1. EMC3–Eirene code

EMC3–Eirene [18, 47] is a steady-state Braginskii plasma fluid solver coupled with a kinetic neutral solver (Eirene [19] that is capable of providing a self-consistent solution of energy, particles and momentum in 3D geometries. For all models, the EMC3–Eirene relies on simplifying assumptions. Although the collisions between particles in the presence of background gradients cause the always present collisional 'classical' transport, it only plays a minor role with respect to the confinement of particles and energy. It is the turbulent, or so called, 'anomalous' transport driven by fluctuations of the plasma parameters, which dominates the perpendicular transport in the SOL. Therefore, the modeling of the perpendicular transport is based on assumptions of a classical diffusion with anomalous diffusion coefficients ($D_\perp$) and anomalous heat conductivity ($\chi_\perp$), which include the turbulent transport. The anomalous transport is also assumed to be of the same magnitude in both perpendicular directions. These coefficients are free model parameters typically obtained by Langmuir probe heat flux measurements in the SOL. For the purposes of this work, $D_\perp = 0.5\mathrm{m}^2\,\mathrm{s}^{-1}$ and $\chi_\perp = 1.5 D_\perp$ were set in order to achieve a compromise between upstream and downstream plasma parameters, as found in previous works [21, 47].

6.2. Results of simulation experiment comparison

For the comparison of MPM probe data with steady-state EMC3–Eirene simulations, we use temporal averaging to remove turbulent fluctuations, which are intrinsically present

in experiments. The time interval of 5 ms was selected as a compromise between an interval long enough for a near steady-state measurement, but short enough for the discharge parameters and probe position to stay relatively constant. Since the measured T_e, n_e follow the normal distribution, a simple mean value is representative for the time interval. In contrast, for the fast BPP T_i time series, the RFA-like averaging technique is found to be a suitable interpretation of fast T_i data for slow time scales, as was also shown in [34]. The MPM data were collected from an upstream main island SOL region $R - R_{LCFS} = 2.5$–3.5 cm from the LCFS. This location was selected to best suit the probe range of motion throughout all the discharges with different line-integrated densities and plasma currents (I_p) while still providing enough data points for good statistics. The MPM data were filtered to best match the input parameters of EMC3–Eirene as follows:

- $P_{ECRH} \in [4, 6]$ MW
- $P_{RAD}/P_{ECRH} \in [0, 0.5]$, that is, well attached divertor conditions.
- $L_c \in [250, 350]$ m, that is, the long connection length region of the island SOL, upstream of divertor targets.
- $I_p \in [-1, 6]$ kA, that is, limited net toroidal plasma current in order to have a relatively well-controlled magnetic island position [43].
- No island manipulation via control coils except for error field correction.

The local plasma parameters (T_e, T_i) obtained from 88 probe insertions during 5 ms intervals satisfying the above listed conditions are plotted against the measured local density n_e in figures 13(a) and (b) as crosses. Plotted in figures 13(c) and (d) are derived parameters $\tau_{i,e} = T_i/T_e$ and the ion-ion collisionality $\nu^*_{ii} = \frac{L_c}{2\lambda_{ii}}$, where the mean free path is $\lambda_{ii} = 10^{16}\frac{T_i^2}{n_e}$. For the fluid approach used in EMC3–Eirene simulations to be valid, the plasma must be collisional ($\nu^*_{ii} \gg 1$). The color of the data points represents the line-integrated density $n_e dl$ of the discharges at the instant of measurement. The $n_e dl$ directly affects the SOL density, as could be seen in figure 12 and is thus left as a free parameter for this scan ranging between 0.1×10^{19} and 10×10^{19} m^{-2}.

EMC3–Eirene calculations were performed for plasma with an input power of $P_{ECRH} = 5$ MW at four different values of the line-integrated density $n_e dl$ corresponding to four local SOL densities of $n_{e,\,SOL} = [0.4, 1.1, 2.2, 2.9] \times 10^{19}$m^{-3}.

The EMC3-Eirene simulations assume a vacuum magnetic field with no toroidal plasma current, $I_p = 0$. In the experiment, plasma currents of up to 6 kA result in a small movement of the LCFS and magnetic island position [43]. Small shifts have been studied in EMC3-Eirene (replicated by introducing around 300 A of planar coil current in the simulations) and did not show qualitatively different simulation results [48]. However, as the fraction of unintersected field lines on the island grows, due to increasing plasma current, qualitative changes in the radiation behavior may start to affect the comparison between simulation and experiment [49]. Because the magnetic geometry is encoded in the grid for EMC3–Eirene calculations, each value of plasma current would, strictly speaking, require its own grid and simulation. Such an exercise is intractable in practice, especially for the small changes in toroidal current discussed here. Assuming that the plasma solution, as modeled by EMC3-Eirene, does not significantly change within the bounds of toroidal current (up to 6 kA), we can emulate the toroidal current effect in the simulation results by varying the radial position of the MPM synthetic diagnostic. This variation is depicted as gray diamonds in figure 13, whereas black diamonds show the $I_p = 0$ case. This gives us an idea for the uncertainty of the EMC3–Eirene estimated plasma parameters when compared to the experimental conditions burdened by both the plasma current and the spatial integration interval of the measurement. Another possible source of error regarding the magnetic field reconstruction is the existence of error fields, which are not assumed in EMC3–Eirene simulations, however these are of secondary importance and their characterization is beyond the scope of this paper.

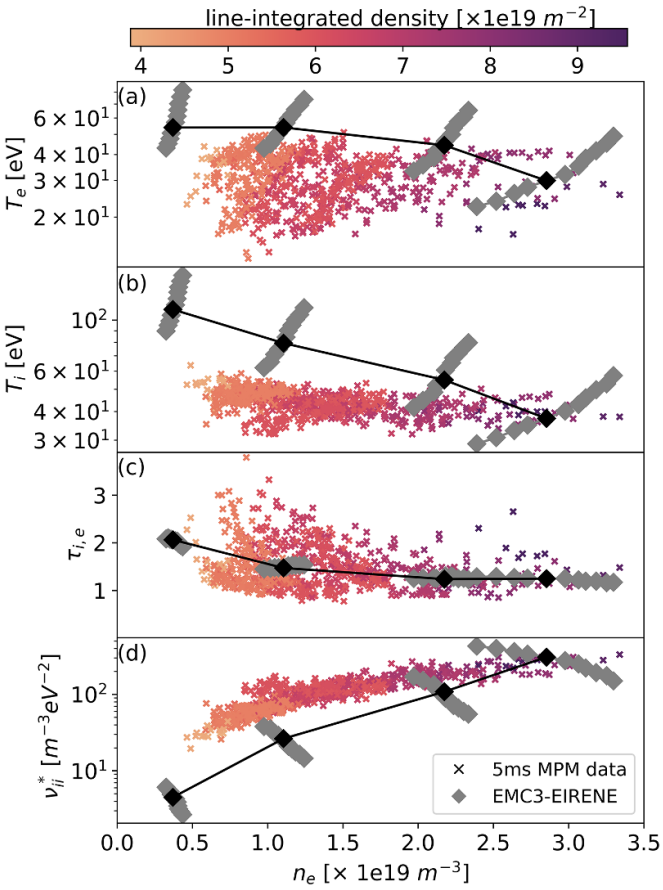

Figure 13. MPM measurements (crosses) and EMC3–Eirene simulations (diamonds) of upstream (a) T_e, (b) T_i, (c) $\tau_{i,e}$, and (d) normalized ion collisionality as a function of upstream n_e. Black diamonds represent simulations for $I_p = 0$ case, gray diamonds represent simulations where toroidal current variations are accounted for.

The experimental results plotted in figures 13(a) and (b), show decrease in both the electron and ion temperature with increasing density and increasing SOL collisionality ν^*_{ii}, plotted in 13(d). While the T_e decreases by a factor of 1.5, the

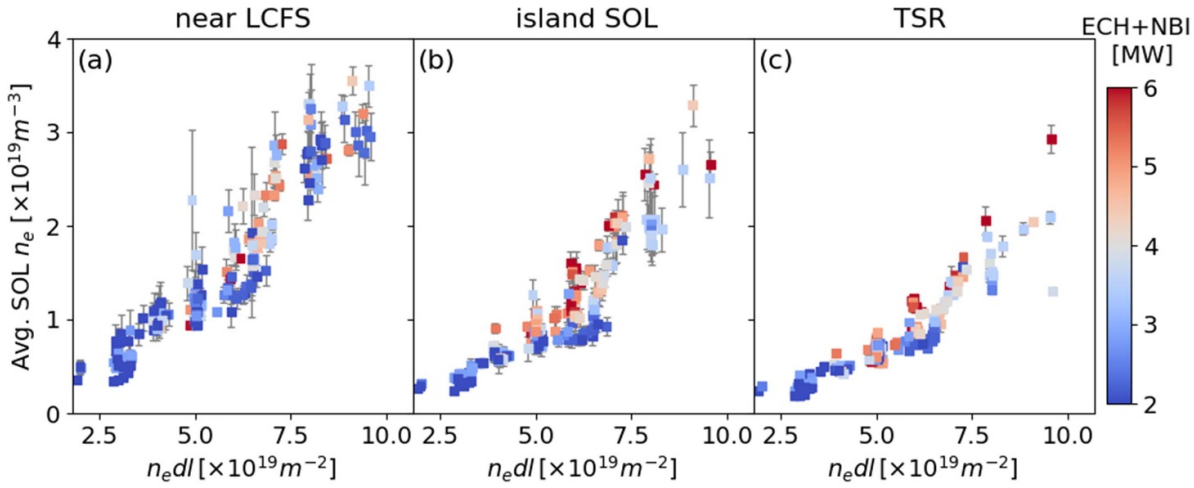

Figure 14. SOL density at three SOL locations as a function of line-integrated density.

T_i decreases by a factor of 2. This is reflected in the $\tau_{i,e}$ in figure 13(c), reaching values of up to 3 in experiment and showing gradual thermalization of ions and electrons up to $\tau_{i,e} = 1$ with the increasing SOL density. Such behavior was previously reported, using RFA in W7-X [14] and in tokamaks [24].

The EMC3–Eirene calculated local plasma parameters (T_e, T_i) and derived SOL quantities ($\tau_{i,e}$ and ν^*_{ii}), shown as diamonds in figures 13(a)–(d) have qualitatively similar trends as the experimental ones. The T_i decreases nearly linearly with the local SOL density (by a factor of ≈ 2.5) and T_e decreases more slowly, similarly to experimental data. The $\tau_{i,e}$ converges to unity with increasing density and increasing normalized SOL collisionality. Quantitatively, the T_i, T_e, $\tau_{i,e}$, and ν^*_{ii} calculated from local EMC3–Eirene results at the highest density match the experiment within the simulation-estimated spatial uncertainty (plasma current effects). However, at the lowest densities T_e and T_i are strongly overestimated when compared to experiment. Interestingly, the $\tau_{i,e}$ still matches the experiment very well, even at the lowest densities. Meaning that, both T_i and T_e, despite having quite different functional dependencies on the density, are offset in such way, that the $\tau_{i,e}$ remains in agreement with experiment. Moreover, the divergence from quantitative agreement to overestimated SOL parameters is gradual. This means that the offset of EMC3-Eirene T_i and T_e values from the experimental ones is systematic, not random. We see that the simulation results gradually begin to diverge around the line-integrated density of $n_e dl \approx 6.5 \times 10^{19}$ m^{-2}. Some possible explanations will be discussed in the following subsection.

6.3. Discussion of simulation-experiment comparison

We first look at the experimental behavior of the SOL profiles as a function of the line-integrated density to provide hints at why the simulations begin to diverge at $n_e dl \approx 6.5 \times 10^{19}$m^{-2}.

Figure 14(a) shows a scan of the local electron density in the SOL regions closest to the LCFS (within 1–2 cm) for varied line-integrated densities. In this region, we observe that with increasing central density, the local density increases nearly linearly. This can be expected, as this region is close to LCFS, where at LCFS a diffusive cross-field transport would be driven by poloidally homogeneous pressure. However, we must note that the probed region being 1–2 cm outside of the LCFS (due to probe limitations) is only an approximation of the LCFS region, where the effects of island SOL transport can already take place. Figures 14(b) and (c) present the same scan for (b) the island SOL and (c) the TSR region. Here, the SOL density clearly exhibits two different linear scalings with $n_e dl$: A weaker linear scaling at low densities and a stronger one at high densities, with a breaking point at $n_e dl \approx 6.5 \times 10^{19}$ m^{-2}. This means that, in the low density regime particles are being transported to the divertor more efficiently (local density profiles are hollow) than in the high density regime (local density profiles are monotonic). This observation implies that a transition in SOL perpendicular transport regimes occurs at a critical density $n_e dl \approx 6.5 \times 10^{19}$ m^{-2}, when the island SOL density reaches $n_e \approx 1.5 \times 10^{19}$ m^{-3}. This observation is further supported by MPM inferred 2D V_{fl} maps of the SOL, where with increasing density, the characteristic magnetic flux-aligned structure of V_{fl} potential, related to the poloidal drifts in the SOL, was seen to weaken at higher densities (see figure 14 in [23]). Interestingly, CIS measurements [50] have shown that as the density increases in the range $n_e dl = 2$–8×10^{19} m^{-2}, the effects of the poloidal $\boldsymbol{E} \times \boldsymbol{B}$ drifts decrease substantially, leading to a reduction in the upper/lower divertor density asymmetry measured by divertor Langmuir probes [51]. The poloidal drift is often thought to be the dominant channel convicting the plasma around the closed field line region of the magnetic island, resulting in the formation of hollow (non-monotonic) temperature profiles [23, 44, 45, 52]. The existence of SOL poloidal drifts has been experimentally proven by a number of diagnostic systems, such as Langmuir probes, gas puff imaging [23] and CIS [50]. Therefore, it is likely that the observed transition in SOL density response is related to a change between a drift dominated regime and a diffusion dominated regime.

We also notice that the input heating power has negligible influence on the SOL density, which also suggests, that the transition at $n_e dl \approx 6.5 \times 10^{19}\,m^{-2}$ is not caused by a nonlinear increase in kinetic pressure at LCFS. Moreover, all the discharges are in the attached divertor regime, thus no transition to detachment is expected to be the cause of the transition. Although, the impurity transport may also play a role, from EMC3–Eirene simulations it is expected that for the range of discharge parameters used here, the impurity transport remains in friction dominated regime, where the friction force exceeds the thermal force and flushes out the impurities outwards keeping them around the targets [4].

The simulation results, shown in figure 13, depend on assumptions about the heat and energy transport using anomalous diffusive transport to describe turbulent transport. For example, the anomalous diffusion coefficient $D_\perp$ and anomalous heat conductivity $\chi_\perp$ were kept constant for the density scan, due to a lack of precise knowledge of the $D_\perp$. Moreover, EMC3–Eirene is missing an implementation of drifts, which are not considered in any of the current 3D codes. Also, as the EMC3–Eirene is an edge code, it does not calculate the core plasma parameters; hence, the line-integrated density in the model is assumed to be a factor of 2 higher than the SOL density. Therefore, as there are multiple factors at play, such as, impurities, neutrals, radiation, drifts and the requirement for nonuniform transport coefficients, it is out of the scope of this paper to discern their individual contributions to the divergence from the experiments.

7. Summary and conclusion

Fast ion temperature measurements in the SOL of W7-X were introduced for the first time, revealing the fine structure of T_i fluctuations and a non-Gaussian PDF. The low background ion temperature is intermittently perturbed by intervals of high T_i, at peaks reaching $\tau_{i,e} = 2-4$. The fast T_i data, averaged using an RFA-like method, are compared with the RFA probe T_i data during similar discharges, showing a good quantitative agreement between the two diagnostics. The averaged T_i profiles are flat with $\tau_{i,e} = 1-3$ in the main SOL and TSR, reaching $T_i = T_e$ in the near LCFS region, where a steep SOL T_e gradient typically occurs. The upstream T_i, obtained with BPP and downstream T_i, inferred by CIS at the divertor target decrease linearly with an increase in central line-integrated density. The downstream ion temperatures are systematically lower than those measured by the BPP RFA-like method. The $\tau_{i,e}$ generally decreases with increasing central line-integrated density. The $\tau_{i,e}$ is, however, also influenced by the input heating power, where a higher input power at the same line-integrated density decreases the T_e profile hollowness near the center of the SOL island and thus decreases the $\tau_{i,e}$. Steady state EMC3–Eirene simulations were performed for an experimentally relevant scenario ($P_{ECH} = 5\,MW$) at a SOL location corresponding to MPM insertion in the island SOL region. EMC3-Eirene has successfully reproduced the qualitative trends observed experimentally in plasmas with similar parameters, such as increase of T_i and $\tau_{i,e}$ with decreasing n_e. In high density plasmas ($n_e dl > 7 \times 10\,m^{-2}$) quantitative agreement between EMC3-Eirene and measurements is observed within the uncertainties of the 'upstream position' and for a default diffusivity, whereas at lower densities the simulations diverge from measurements. The divergence at low densities is potentially attributable to SOL drift flows, which are not included in EMC3-Eirene. Such flows have been observed to have a significant SOL transport contribution [50, 51] and are considered to be responsible for non-monotonic T_e profiles in the SOL [23, 45]. The impact of these drift flows has been shown to substantially decrease for higher plasma densities, potentially explaining the better agreement between experiment and EMC3–Eirene simulations at high densities.

Data availability statement

The data cannot be made publicly available upon publication due to legal restrictions preventing unrestricted public distribution. The data that support the findings of this study are available upon reasonable request from the authors.

Acknowledgments

The authors thank J Cavalier for insightful discussions. This work has been carried out within the framework of the EUROfusion Consortium, funded by the European Union via the Euratom Research and Training Programme (Grant Agreement No 101052200 — EUROfusion). Views and opinions expressed are however those of the author(s) only and do not necessarily reflect those of the European Union or the European Commission. Neither the European Union nor the European Commission can be held responsible for them.

ORCID iDs

Dario Cipciar 0000-0002-3798-9524
Jiri Adamek 0000-0001-8562-1233
Carsten Killer 0000-0001-7747-3066
David Matthew Kriete 0000-0002-3657-2911
Victoria Winters 0000-0001-8108-7774
Valeria Perseo 0000-0001-8473-9002
Olaf Grulke 0000-0001-7879-8671
Alexander Knieps 0000-0003-0083-7188

References

[1] König R *et al* 2002 *Plasma Phys. Control. Fusion* **44** 2365
[2] Pedersen T S *et al* 2022 *Nucl. Fusion* **62** 042022
[3] Feng Y 2022 *Plasma Phys. Control. Fusion* **64** 125012
[4] Feng Y, Kobayashi M, Lunt T and Reiter D 2011 *Plasma Phys. Control. Fusion* **53** 024009
[5] Stephey L *et al* 2018 *Phys. Plasmas* **25** 062501
[6] Effenberg F *et al* 2019 *Nucl. Mater. Energy* **18** 262–7
[7] Pedersen T S *et al* 2019 *Nucl. Fusion* **59** 096014
[8] Chaudhary N, Hirsch M, Andreeva T, Geiger J, Wolf R C and Wurden G A 2024 *Nucl. Fusion* **64** 106038
[9] Vuoriheimo T *et al* 2024 *Nucl. Mater. Energy* **41** 101766
[10] Al-Malkawi G H, Al-Ajlony A-M B A and Al-Shboul K F 2023 *Nucl. Mater. Energy* **35** 101442

[11] Adamek J *et al* 2016 *Rev. Sci. Instrum.* **87** 043510
[12] Adamek J *et al* 2021 *Nucl. Fusion* **61** 036023
[13] Birkenmeier G *et al* 2015 *Nucl. Fusion* **55** 033018
[14] Li Y *et al* 2019 *Nucl. Fusion* **59** 126002
[15] Henkel M *et al* 2020 *Fusion Eng. Des.* **157** 111623
[16] Kriete D M, Perseo V, Gradic D, Ennis D A, König R and Maurer D A 2024 *Rev. Sci. Instrum.* **95** 073503
[17] Gradic D , Krychowiak M, König R, Henke F, Otte M, Perseo V and Pedersen T S 2022 *Plasma Phys. Control. Fusion* **64** 075010
[18] Feng Y *et al* 2014 *Contrib. Plasma Phys.* **54** 426–31
[19] Reiter D, Baelmans M and Börner P 2005 *Fusion Sci. Technol.* **47** 172–86
[20] Winters V R *et al* 2021 *Plasma Phys. Control. Fusion* **63** 045016
[21] Winters V R *et al* 2024 *Nucl. Fusion* **64** 126047
[22] Killer C, Drews P, Grulke O, Knieps A, Nicolai D and Satheeswaran G 2022 *J. Instrum.* **17** 03018
[23] Killer C , Cipciar D, Baek S G, Ballinger S B, Stechow A V, Terry J L and Grulke O 2025 *Nucl. Fusion* **65** 056026
[24] Kocan M , Gunn J P, Pascal J-Y, Bonhomme G, Fenzi C, Gauthier E and Segui J-L 2008 *Plasma Phys. Control. Fusion* **50** 125009
[25] Grenfell G *et al* 2022 *Rev. Sci. Instrum.* **93** 023507
[26] Hey J D, Chu C C, Brezinsek S, Mertens P and Unterberg B 2002 *J. Phys. B: Atom. Mol. Opt. Phys.* **35** 1525
[27] Gradic D *et al* 2021 *Nucl. Fusion* **61** 106041
[28] Feng Y, Sardei F, Grigull P, McCormick K, Kisslinger J and Reiter D 2006 *Nucl. Fusion* **46** 807
[29] Hey J D , Chu C C, Mertens P, Brezinsek S and Unterberg B 2004 *J. Phys. B: At. Mol. Opt. Phys.* **37** 2543
[30] Desideri D Serianni G 1998 *Rev. Sci. Instrum.* **69** 2354–6
[31] Murphy-Sugrue S , Harrison J, Walkden N R, Bryant P and Bradley J W 2017 *Plasma Phys. Control. Fusion* **59** 055007
[32] Stangeby P C *et al* 1990 *Nucl. Fusion* **30** 1225
[33] Ochoukov R *et al* 2020 *Rev. Sci. Instrum.* **91** 063506
[34] Cipciar D, Adamek J, Horacek J, Cavalier J and Hron M 2022 *Plasma Phys. Control. Fusion* **64** 055021
[35] Nielsen H *et al* 2017 *Plasma Phys. Control. Fusion* **59** 025012
[36] Kocan M *et al* 2011 *J. Nucl. Mater.* **415** 1133–8
[37] Redl A *et al* 2024 *Nucl. Fusion* **64** 086064
[38] Killer C, Shanahan B, Grulke O, Endler M, Hammond K and Rudischhauser L 2020 *Plasma Phys. Control. Fusion* **62** 085003
[39] Cipciar D *et al* 2025 *Nucl. Fusion* **65** 046010
[40] Rahbarnia K *et al* 2018 *Nucl. Fusion* **58** 096010
[41] Valsaque F, Manfredi G, Gunn J P and Gauthier E 2002 *Phys. Plasmas* **9** 1806–14
[42] Dreval M , Rohraff D, Xiao C and Hirose A 2009 *Rev. Sci. Instrum.* **80** 103505
[43] Killer C *et al* 2019 *Plasma Phys. Control. Fusion* **61** 125014
[44] Barbui T *et al* 2020 *Nucl. Fusion* **60** 106014
[45] Flom E *et al* 2024 Observation of a drift-driven transport regime in the island divertor of Wendelstein 7-X (arXiv:2312.01240)
[46] Killer C, Narbutt Y and Grulke O (W7-X Team) 2021 *Nucl. Fusion* **61** 096038
[47] Feng Y *et al* 2021 *Nucl. Fusion* **61** 106018
[48] Feng Y 2021 *Nucl. Fusion* **61** 086012
[49] Feng Y , Beidler C D, Geiger J, Helander P, Hölbe H, Maassberg H, Turkin Y and Reiter D 2016 *Nucl. Fusion* **56** 126011
[50] Kriete D M *et al* 2023 *Nucl. Fusion* **63** 026022
[51] Hammond K C *et al* 2019 *Plasma Phys. Control. Fusion* **61** 125001
[52] Kraemer-Flecken A *et al* 2019 *Plasma Phys. Control. Fusion* **61** 054003